Hyperspectral imagery and LiDAR for Geological Analysis of Cuprite, Nevada

Michael S. West[a*] and Ronald G. Resmini[b†]

[a] The MITRE Corporation, M/S T630, 7515 Colshire Dr., McLean, VA 22102, USA;
[b] The National Geospatial Intelligence Agency, Basic and Applied Research Office (IB)
12310 Sunrise Valley Drive, MS P-129, Reston, Virginia 20191, USA

ABSTRACT

Fusion of Light Detection and Ranging (LiDAR) and Hyperspectral Imagery (HSI) products is useful for geological analysis, particularly for visualization of geomorphology and hydrology. In early 2007, coincident hyperspectral imagery and LiDAR were acquired over Cuprite, Nevada. The data were analyzed with ENVI and the ENVI LiDAR Toolkit. Results of the analysis of these data suggest, for some surfaces, a correlation between mineral content and surface roughness. However, the LiDAR resolution (~1 meter ground sampling distance) is likely too coarse to extract surface texture properties of clay minerals in some of the alluvial fans captured in the imagery. Though not demonstrated in this particular experiment (but a goal of the research), the relation between surface roughness and mineral composition may provide valuable information about the mechanical properties of the surface cover—in addition to generating another variable useful for material characterization, image classification, and scene segmentation. Future mission planning should include consideration of determining optimal ground sampling to be used by LiDAR and HSI systems. The fusion of LiDAR elevation data and multi- and hyperspectral classification results is, in and of itself, a valuable tool for imagery analysis and should be explored further.

Keywords: hyperspectral, lidar, spectroscopy, Cuprite, HSI, geology, surface roughness, alluvial fan, mineral content

1. INTRODUCTION

The utility of fusing hyperspectral imagery (HSI) and Light Detection and Ranging (LiDAR) has been demonstrated for the analysis of vegetation[1]. It was shown that fusing surface roughness derived from LiDAR and matched filter scores from HSI improved the classification of sagebrush in arid regions. It has also been demonstrated that LiDAR is useful for characterizing the surface roughness of alluvial fan regions[2]. This paper addresses the question of whether a similar approach can be used to improve mineral mapping and characterizing mechanical properties of rocks via spectral remote sensing. We will explore the hypothesis that surface roughness derived from LiDAR returns is correlated with the mineral composition derived from VNIR/SWIR (0.4 μm to 2.5 μm) hyperspectral imagery.

2. MATERIALS AND METHODS

A total of 14 passes were made over and to the west of the Cuprite mining district in southwest Nevada, spanning an area of approximately 108 square kilometers from an altitude of 2.23 kilometers above sea level. Cuprite encompasses an area of hydrothermally altered and unaltered exposed rocks. Previous studies[3-8] of this site have identified silicified regions of predominantly quartz with minor alunite ($KAl_3(SO_4)_2(OH)_6$), kaolinite ($Al_2Si_2O_5(OH)_5$), and calcite ($CaCO_3$); opalized areas containing alunite, disseminated opal ($SiO_2{\cdot}nH_2O$), calcite replacing opal, and kaolinite; and argillized regions of primarily kaolinite with montmorillonite ($(Na,Ca)_{0.33}(Al,Mg)_2(Si_4O_{10})(OH)_2{\cdot}nH_2O$) and minor opal. The area of interest for this study is the alluvial fan around the two alunite-rich mounds near 37° 31' 28.79" N, 117° 12' 44.61" W, which is to the west of the US-95 road. The mean elevation of the site is 1.55 kilometers above sea level.

Data were collected over the site using a suite of sensors on board a DC3 aircraft operated by Airborne Imaging, which included the Mapping Reflected-energy Spectrometer (MaRS), a Nikon™ D2X camera, and an Optech LiDAR. MaRS is an HSI sensor built by NASA JPL that measures spectra in the 0.4 μm to 2.5 μm spectral range. The Nikon™

* Contact information: (703) 983-6880, mwest@mitre.org
† Contact information: (703) 735-2793, Ronald.G.Resmini@nga.mil or rresmini@gmu.edu

D2X is a digital SLR camera that was used for capturing high spatial resolution true color imagery. The LiDAR system operates with a wavelength of 1.064 μm.

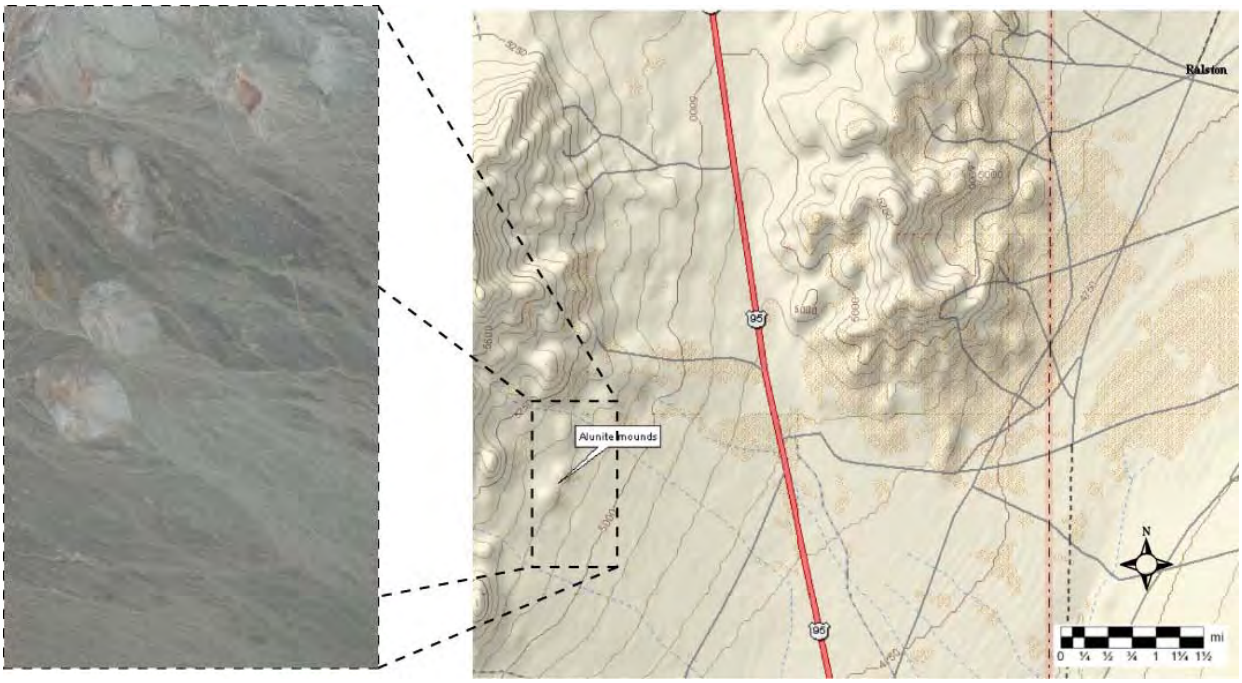

Figure 1 Mosaic of Nikon true color imagery (left) over the area of interest (outlined on the map). (Map credit: © 2004 DeLorme (www.delorme.com) Topo USA®.)

One data set covering the area of interest was chosen from each of the two sensors. The ground sampling distances (GSD) at the relative altitude above the ground for each sensor was approximately 1 meter for LiDAR and 0.68 meter for MaRS. The entire flight line covered an area of 5.4 square kilometers, while the region of interest covered only 1.5 square kilometers. Therefore, spatial subsets of LiDAR and MaRS imagery were created over the region of interest to reduce processing time.

MaRS data were converted from radiance to reflectance using in-scene information and a simplified sensor model[9] where the at-sensor radiance in the i^{th} band, L_i, was approximated by a simple gain, G, multiplied by the target reflectance, ρ_i, and added to an offset term, P,

$$L_i = G\rho_i + P\,. \tag{1}$$

The offset, P, or "path radiance", is estimated by finding the band-minimums for the entire datacube. In-scene regions of interest (ROI's) of the alunite mounds and the United States Geological Survey (USGS) spectrum for alunite[10] were used to estimate the multiplicative gain term, G. The ROI's were selected based upon previous mineral mapping work by Resmini et al.[11] and the USGS[12]. The radiance data were then converted to reflectance by inverting Equation (1) to solve for the target reflectance, ρ_i,

$$\rho_i = \frac{L_i - P}{G}\,. \tag{2}$$

Attempts to use the physics-based algorithm FLAASH[13] failed due to the presence of clouds overhead at the time of the data collection.

Linear spectral mixture analysis[14,15,16] of the MaRS reflectance imagery was then performed using the 2.0 μm – 2.5 μm region of the spectrum, which is a "fingerprint" region of the solar reflective spectrum for minerals. The model used

for this analysis assumes that each pixel is an areal mixture of the dominant minerals such that the pixel reflectance is simply a weighted sum of the reflectance of each constituent spectral endmember (wavelength dependence implied)

$$\rho_{image} = \sum_j \alpha_j \cdot \rho_j + E, \tag{3}$$

where α_j is the relative abundance of the material with reflectance ρ_j, and E is the RMS error between the model and the data. Furthermore, the model is constrained such that α_j is positive for all j and the endmembers sum to 1. Spectral endmembers were selected from the scene that closely matched spectra from a previous USGS study cited above. The results were saved as single-band fraction plane images scaled to the relative abundance of each mineral used for the mixture analysis.

Surface roughness was computed from the LiDAR imagery, where roughness is defined as the standard deviation of the height distribution in the neighborhood of each pixel[17]. Like the abundance fraction planes from the spectral mixture analysis, the surface roughness results were saved as single-band gray-scaled images. The fraction plane and roughness images were then georeferenced and layer-stacked. Scatter plot analysis was used to qualitatively evaluate the correlation between the LiDAR and HSI products.

3. RESULTS AND DISCUSSION

False color composites of the region of interest were generated from the MaRS and LiDAR imagery to provide a general overview of the material distribution around the alunite mounds, as shown in Figure 2. The alluvial flow channels are very distinct in the LiDAR intensity image, fanning out from West to East, which is the direction of descending altitude from the alunite mounds. The color space distribution in the MaRS SWIR false color image suggests that the composition in the region can be represented by a small (3-5) endmember spectral mixture model. Iterative in-scene user-selected endmember linear unmixing converged on a 3-endmember mixture model. The three endmembers were matched to the USGS mineral library and identified as alunite, montmorillonite, and kaolinite-smectite (a.k.a. "kaosmec"). The fraction planes and RMS image are shown in Figure 3.

Figure 4 shows a false-color RGB image of the stacked fraction planes overlaid on a digital surface model generated from the LiDAR image. The fusion of hyperspectral and LiDAR data provides a useful means for visualizing the distribution of material and hydrology. Alunite typically occurs in the environment as massive structures[18], which are easily identifiable in this scene as large mounds. Note that the deep channels in the alluvial fan correlate to a high abundance of the montmorillonite, which is a clay mineral of altered volcanic ash. The more elevated regions are composed of kaolinite and smectite, which are also clay minerals formed by the weathering and hydrothermal alteration of silicates.

The brighter material in the alluvial fan regions observed in the Nikon context (Figure 1) and the LiDAR intensity images (Figure 2) correspond to the montmorillonite spectral detections. This relative brightness is consistent with the assumption of small grain sizes in the alluvial channels, as compared to darker regions[19]. However this does not bear out in the LiDAR surface roughness products. Clay minerals are comprised of fine particles on the order of 1 micrometer. Therefore, they would not be expected to exhibit much in the way of surface roughness as measured by LiDAR with a 1 meter GSD. This appears to be the case when examining the absolute and local surface roughness LiDAR products, as shown in Figure 5.

Absolute and local surface roughness differ only in that the slope is removed from the absolute surface roughness to calculate the local roughness. Thus the local surface roughness captures the vegetation (seen as speckles throughout the scene), the sides of the deep channels, and areas of high roughness on the alunite mounds. At a LiDAR resolution of 1 meter, there may be only a weak correlation between the mineral abundance and surface roughness, as evidenced by the seemingly random distribution of points in the scatter plots shown in Figure 6, Figure 7, and Figure 8. The distribution functions of absolute and local surface roughness values appear to be unimodal (Figure 9), while the distribution functions of mineral abundances appear to be bimodal (Figure 10), with purest abundances being that of alunite.

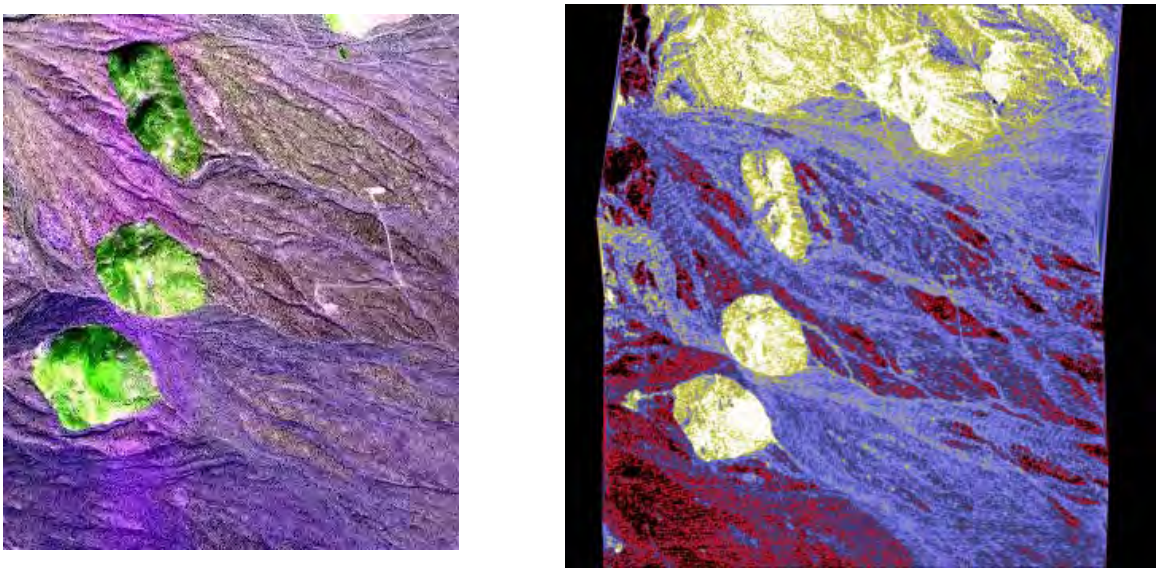

Figure 2 False color composites derived from MaRS (left) and LiDAR (right). The MaRS image is formed from a combination of three spectral bands: 2.43 μm (red), 2.35 μm (green), and 2.16 μm (blue). The LiDAR image is the intensity of return signal scaled to the Rainbow color map.

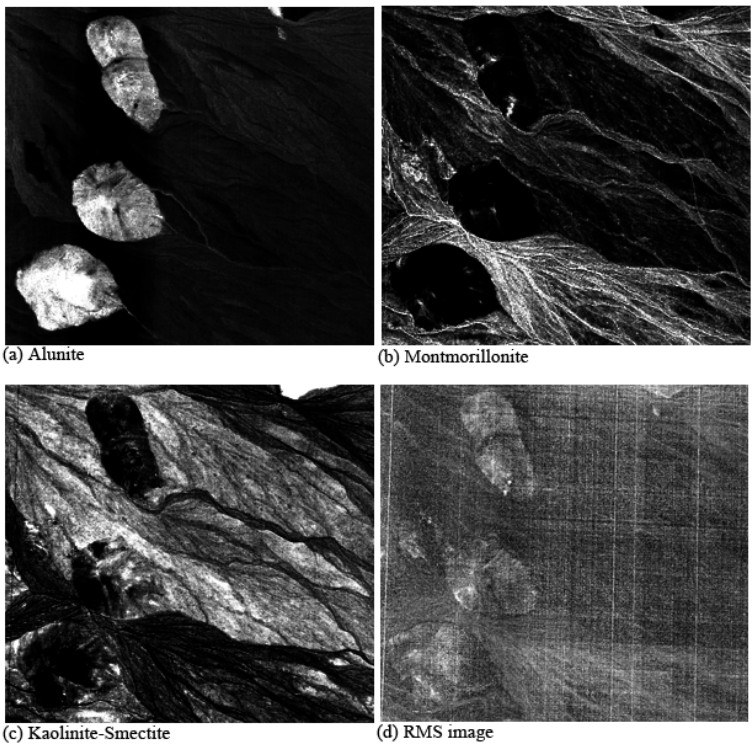

Figure 3 Fraction planes and their associated mineral spectra used for unmixing the hyperspectral data.

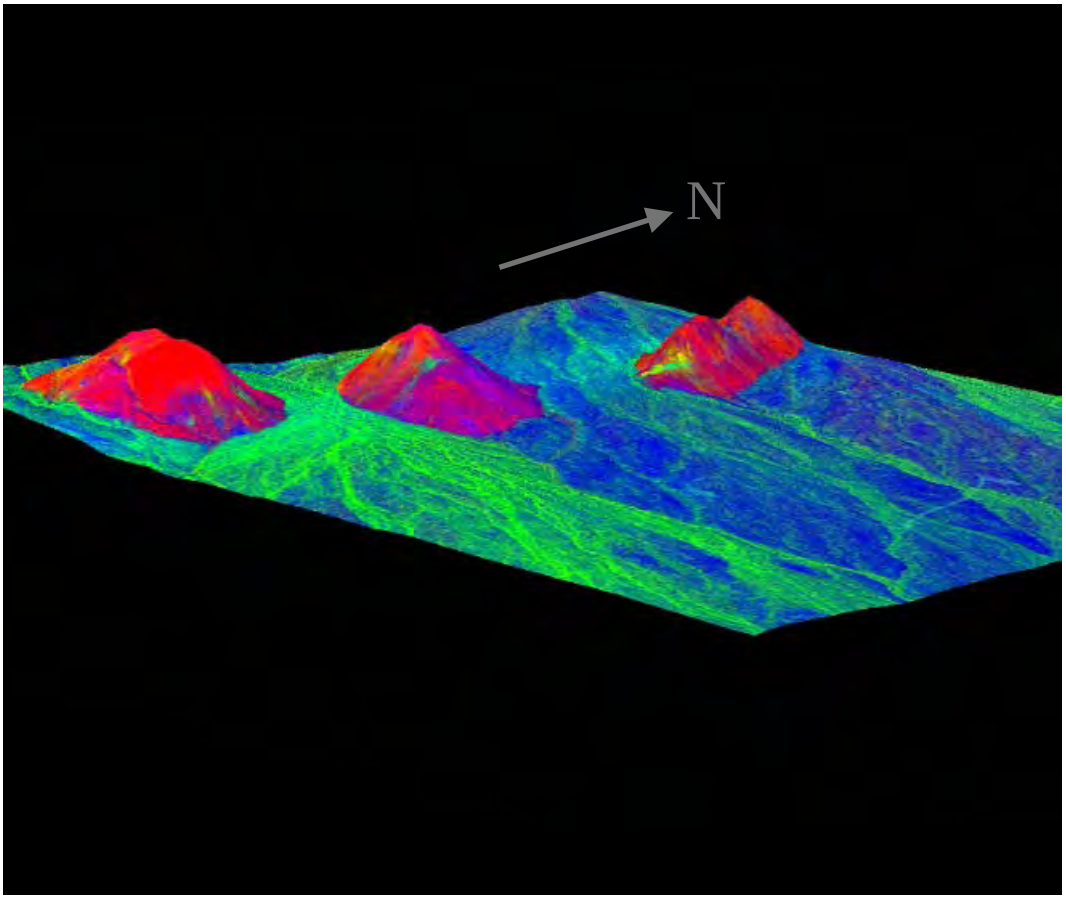

Figure 4 False color RGB image formed by three fraction planes overlaid on a digital surface model. The height is exaggerated by a factor of 3. Each color corresponds to the abundance of a particular mineral: alunite (red); montmorillonite (green); and kaolinite-smectite (a.k.a. "kaosmec") (blue).

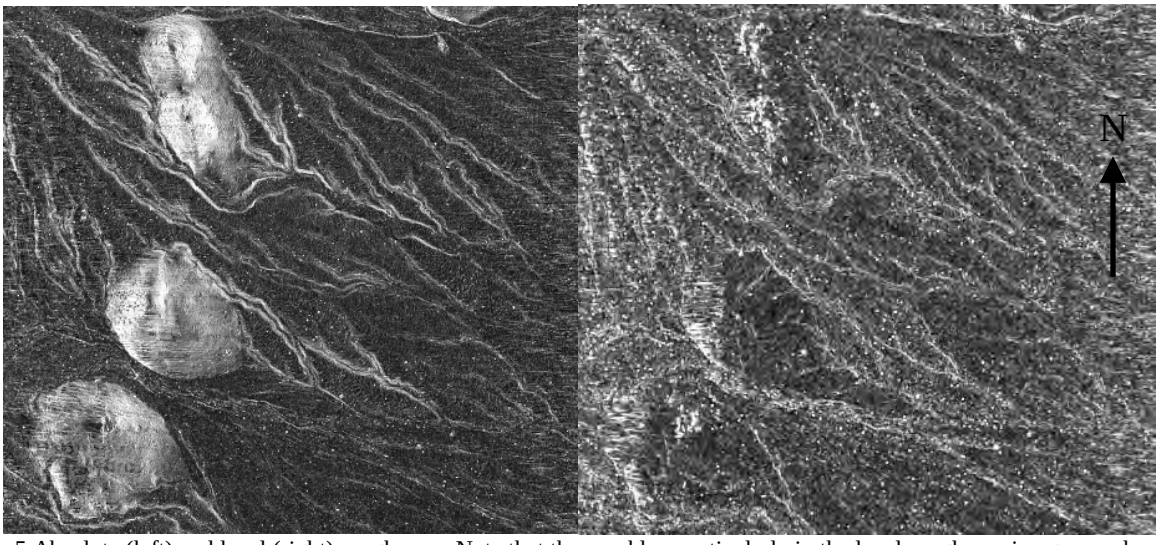

Figure 5 Absolute (left) and local (right) roughness. Note that the speckles, particularly in the local roughness image, are due to vegetation.

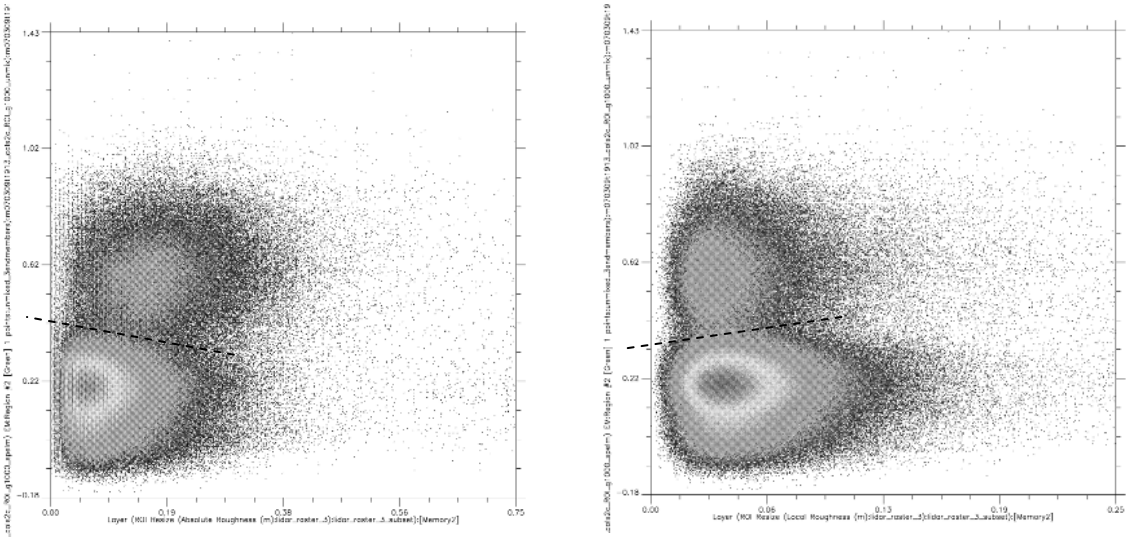

Local Roughness (m) Absolute Roughness (m)

Figure 6 Alunite abundance plotted against the local and absolute roughness. The dotted line indicates the boundary between pure alunite and everything else in the scene.

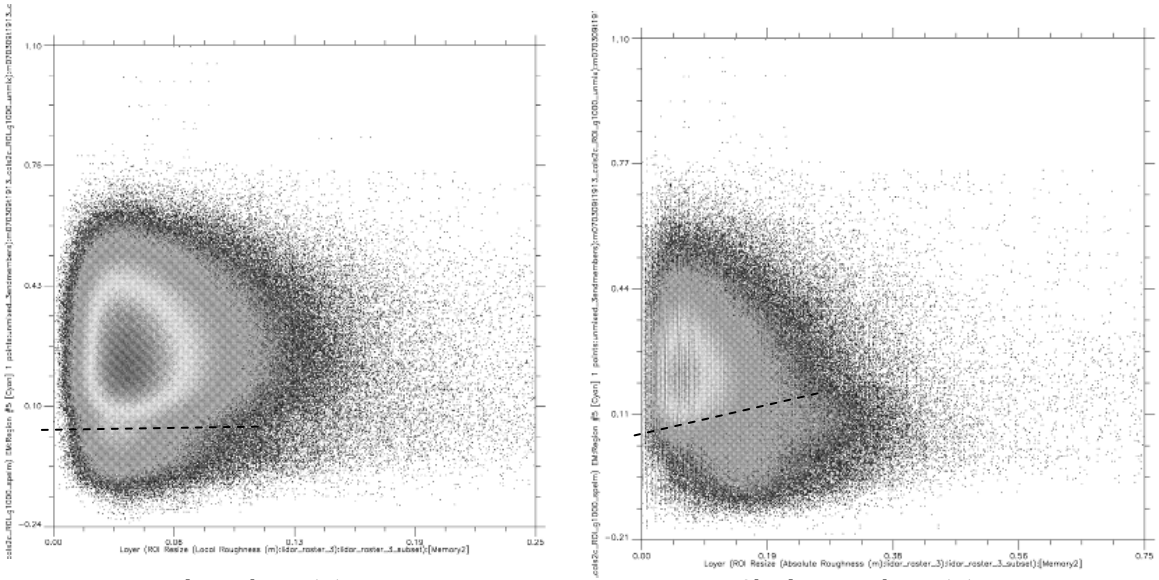

Local Roughness (m) Absolute Roughness (m)

Figure 7 Montmorillonite abundance versus surface roughness.

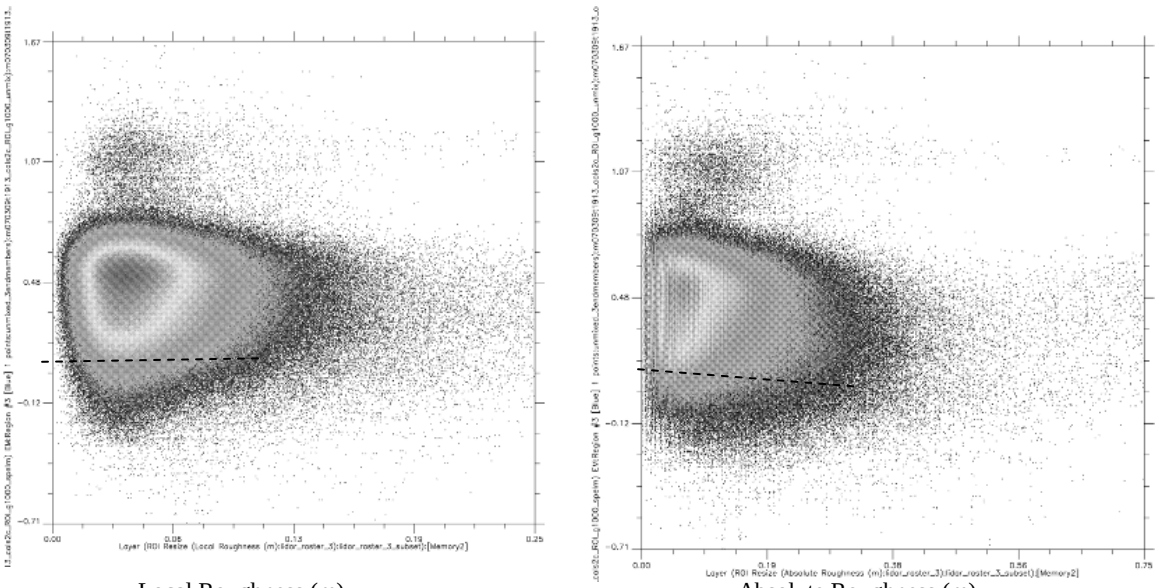

Local Roughness (m) Absolute Roughness (m)

Figure 8 Kaolinite-smectite abundance versus surface roughness.

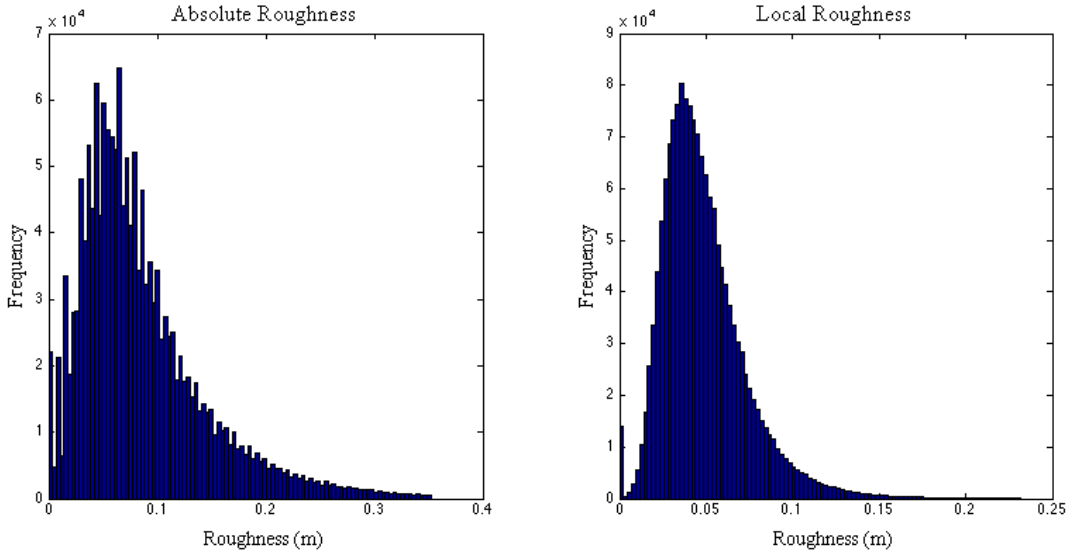

Figure 9 Distributions of the absolute (left) and local (right) surface roughness values measured over the entire area of interest.

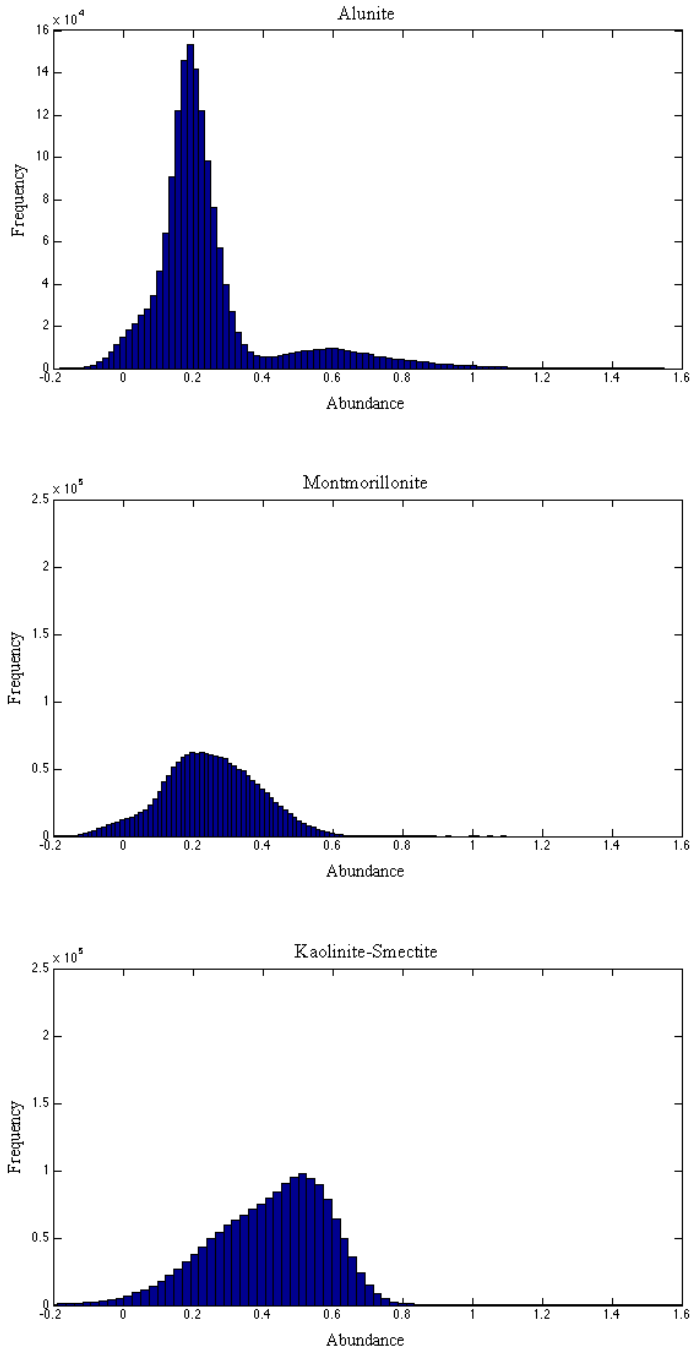

Figure 10 Distribution of the abundances for alunite (top), montmorillonite (middle), and kaolinite-smectite (bottom). The alunite is strongly bimodal, while the montmorillonite and kaolinite-smectite distributions are weakly bimodal with large regions of overlap.

4. CONCLUSIONS

Fusion of LiDAR and HSI products is useful for geological analysis, particularly for visualization of geomorphology and hydrology. Results of this analysis suggest that there *may* be a correlation between mineral content and surface roughness. However, the LiDAR resolution (~1 m GSD) is too coarse to extract surface properties of clay minerals in the alluvial fan from this data collection. The methods and procedures demonstrated in this analysis may be used on other data sets to more rigorously test the hypothesis.

Though it was not demonstrated in this particular experiment, the relation between surface roughness and mineral composition can provide valuable information about the mechanical properties of rocks and soils. Future aerial surveys should take into consideration flight parameters required to obtain the optimal ground sampling used by both LiDAR and hyperspectral imaging systems. The fusion of LiDAR elevation data and multi- and hyperspectral classification results is in and of itself a valuable tool for imagery analysis and should be explored further.

REFERENCES

1. Mundt J. T., Streutker D. R., and Glenn N. F. Mapping Sagebrush Distribution Using Fusion of Hyperspectral and Lidar Classifications, *Photogrammetric Engineering & Remote Sensing*, pp. 47-54, January 2006.
2. Frankel, K. L and Dolan, J. F., Characterizing arid region alluvial fan surface roughness with airborne laser swath mapping digital topographic data, *Journal of Geophysical Research*, Vol. 112, May 2007.
3. Abrams, M. J., Ashley, R. P., Rowan, L. C., and Geotz, A. F. H., Mapping of hydrothermal alteration in the Cuprite mining district, Nevada, using aircraft scanner images for the spectral region 0.46 to 2.36 ㎜, *Geology*, 5, pp. 713-718, 1977.
4. Abrams, M. J., Ashley, R. P., Rowan, L. C., Geotz, A. F. H., and Kahle, A. B., Use of imaging in the 0.46-2.36 μm spectral region for alteration mapping in the Cuprite mining district, Nevada. United States Geological Survey Open-File Report, 77-585, 1977.
5. Curtiss, B., Smith, M. O., and Adams, J. B., Separation of hydrothermal Fe(III) oxyhydroxides from weathering produced Fe(III) oxyhydroxides in multispectral images, *Fourth Thematic Conference: Remote Sensing for Exploration Geology, San Francisco* (Ann Arbor, Michigan: Environmental Research Institute of Michigan), 1985.
6. Goetz, A. F. H., and Rowan, L. C., Geologic remote sensing, *Science*, 211, 781-791, 1981.
7. Goetz, A. F. H., and Srivastava, V., Mineralogical mapping in the Cuprite mining district, *Proceedings of the Airborne Imaging Spectrometer (AIS) Data Analysis Workshop, Pasadena, 8-10 April 1985*, Jet Propulsion Laboratory Publication 85-41 (Pasadena, California: JPL), pp. 22-29, 1985.
8. Goetz, A. F. H., Vane, G., Solomon, J. E., and Rock, B. N., Imaging spectrometry for earth remote sensing, *Science*, 228, pp. 1147-1153, 1985.
9. Roberts D. A., Yamaguchi, Y., and Lyon, R. J. P., Comparison of various techniques for calibration of AIS data. *Second Airborne Imaging Spectrometer Data Analysis Workshop*, JPL publication 86-35 (Pasadena, CA: Jet Propulsion Laboratory), pp. 21-30.
10. Clark, R.N., G.A. Swayze, A.J. Gallagher, T.V.V. King, and W.M. Calvin, 1993, The U. S. Geological Survey, Digital Spectral Library: Version 1: 0.2 to 3.0 microns, *U.S. Geological Survey Open File Report 93-592*, 1340 pages.
11. Resmini R. G., Kappus M. E., Aldrich W. S., Harsanyi J. C., and Anderson M. Mineral mapping with HYperspectral Digital Imagery Collection Experiment (HYDICE) sensor data at Cuprite, Nevada, U.S.A. *International Journal of Remote Sensing*, 1997, Vol. 18, No. 7, pp. 1553-1570.
12. Clark R. N., Swayze G. A., Livo E., Kokaly R. F., Sutley S. J., Dalton J. B., McDougal R. R., and Gent C. A. Imaging spectroscopy: Earth and planetary remote sensing with USGS Tetracorder and expert systems, *Journal of Geophysical Research*, Vol. 108, No. E12, 2003.
13. Adler-Golden S. M. et al, Atmospheric Correction for Short-wave Spectral Imagery Based on MODTRAN4, in *SPIE Proceedings, Imaging Spectrometry V*, Volume 3753, SPIE 1999.
14. Schowengerdt, R. A., *Remote Sensing: Models and Methods for Image Processing*, Chapter 9, pp. 447-455, Academic Press, San Diego, 1997.
15. Adams, J. B., and Gillespie, A. R., *Remote Sensing of Landscapes with Spectral Images: A Physical Modeling Aproach*, Chapter 4, Cambridge University Press, Cambridge, 2006.

16. Adams, J.B., Smith, M.O., and Gillespie, A.R., (2003). Imaging spectroscopy: interpretation based on mixture analysis. *In: Remote Geochemical Analysis: Elemental and Mineralogical Composition, Topics in Remote Sensing 4*, Pieters, C.M., and Englert, P.A.J., eds., Cambridge, University Press, p. 145-166.
17. Lausten, K. M., ENVI LiDAR Toolkit, http://www.ittvis.com, 2007.
18. Klein, Cornelis, *The 22nd Edition of the Manual of Mineral Science*, John Wiley and Sons, 1977.
19. Hapke, B., *Introduction to the Theory of Reflectance and Emittance Spectroscopy*, Cambridge University Press, New York, 1993.